

Defect Physics of Ternary Semiconductor ZnGeP_2 with a High Density of Anion-Cation Antisites: A First-Principles Study

Menglin Huang,¹ Shan-Shan Wang,¹ Yu-Ning Wu,^{1,*} and Shiyou Chen^{1,2,†}

¹Key Laboratory of Polar Materials and Devices (MOE), East China Normal University, Shanghai 200241, China

²State Key Laboratory of ASIC and System, School of Microelectronics, Fudan University, Shanghai 200433, China



(Received 5 November 2020; revised 5 January 2021; accepted 21 January 2021; published 16 February 2021)

Anion-cation antisite defects usually have low density in the group III-V (e.g., GaN) and II – IV – V₂ (ZnGeN_2 , ZnSnP_2) semiconductors, and thus, have not drawn enough attention in defect studies of ZnGeP_2 since 1976. However, our first-principles calculations based on a hybrid functional show that the anion-cation antisite defects (Ge_P and P_Ge) can have very high density ($10^{17} – 10^{18} \text{ cm}^{-3}$), making them the dominant defects in ZnGeP_2 . Their calculated photoluminescence (PL) spectra agree well with the 1.4 and 1.6 eV PL peaks observed experimentally, indicating that they may be the origin of defects, which challenges previous assumptions that the P vacancy (V_P) defect is responsible for the two PL peaks. Although the anion-cation antisites (Ge_P and P_Ge) and cation-cation antisites (Ge_{Zn} and Zn_{Ge}) both have densities as high as 10^{17} cm^{-3} , ZnGeP_2 suffers from serious donor-acceptor compensation, which results in a low carrier density (below 10^{10} cm^{-3}), and thus, poor electrical conductivity. These results explain the mysterious observation that ZnGeP_2 crystals grown using different methods have a high defect density, but low carrier density and high resistivity, and also indicate that it is challenging to suppress the defect-induced optical absorption in the development of high-power ZnGeP_2 -based optical devices.

DOI: 10.1103/PhysRevApplied.15.024035

I. INTRODUCTION

ZnGeP_2 is a group II-IV-V₂ semiconductor in the chalcopyrite structure, which can be derived from the binary zinc blende-structured GaP via cation mutation, i.e., replacing the group III cation Ga^{3+} with group II Zn^{2+} and group IV Ge^{4+} . It is one of the most promising infrared nonlinear optical materials that can be used for frequency conversion, second-harmonic generation (SHG), and optical parametric oscillator (OPO), owing to its large nonlinear optical coefficient, high thermal conductivity, and sufficient birefringence [1–16].

In the development of high-power ZnGeP_2 -based optical devices, the presence of point defects in the crystals is a serious limiting factor, e.g., although the material is relatively transparent for the 0.7–2.5 μm light, there is still a broad defect-related absorption band [17–25]. It is reported that the density of both the donor and acceptor defects can be as high as 10^{19} cm^{-3} [26,27], indicating that the influences of point defects can be significant. Interestingly, despite such a high density of defects, the electrical conductivity of crystals grown is very poor. A ZnGeP_2 crystal can be grown using the Bridgman method

[28,29] or high-pressure physical vapor transport (HPVT) [19,30]. Bridgman-grown ZnGeP_2 exhibits *p*-type conductivity with a low hole density of 10^{10} cm^{-3} [31–33], whereas HPVT-grown ZnGeP_2 is reported to show *n*-type conductivity with high resistivity [19,30].

To understand the origin of the broad defect-related absorption band and high resistivity, both experimental and theoretical techniques are adopted to study the point defects in ZnGeP_2 [17–19,34–47]. Electron paramagnetic resonance (EPR) [17,35–39] and photo-EPR [34,36–39] studies detect three major defect signals, namely, two donors, which are presumably attributed to V_P and Ge_{Zn} [17,34], and one acceptor, which is attributed to V_{Zn} or Zn_{Ge} [35], based on the measured *g* matrix and hyperfine interaction. The photoluminescence (PL) spectra show that Bridgman-grown *p*-type ZnGeP_2 exhibits three different PL peaks at around 1.23 [40], 1.4 [23,41], and 1.6 eV [23,31,40,41,47], while the HPVT-grown crystals have an exclusive emission at 1.2 eV [19,47]. According to the EPR and photo-EPR results, both the 1.4 and 1.6 eV PL peaks are attributed to the P vacancy (V_P) defect [23,41], while the 1.2 eV emission is attributed to the antisite on cation sites (Ge_{Zn}) [19]. Theoretically, Jiang *et al.* calculated the formation energies of five point defects, V_{Zn} , V_{Ge} , Ge_{Zn} , Zn_{Ge} , and V_P to try to explain the PL peaks and EPR signals corresponding to these defects, and found that

*ynwu@phy.ecnu.edu.cn

†chensy@fudan.edu.cn

Ge_{Zn} had a low formation energy and could act as a *p*-type limiting defect [43–46].

Despite these pioneering studies, the defect physics in ZnGeP_2 is not yet well understood. An early EPR study in 1976 mentioned an anion-cation antisite defect, presumably the neutral P_{Ge} antisite [48]. Surprisingly, the anion-cation antisite defects had neither been observed in a large number of experimental studies in the following decades [17–19,34–42], nor considered in first-principles calculation studies [43–46,49,50], so it is unclear whether these antisites exist or have high density in the ZnGeP_2 crystals grown. Most of the previous defect studies focused on point defects, such as V_{Zn} , V_{Ge} , Ge_{Zn} , Zn_{Ge} , and V_{P} . In fact, such kinds of defects (vacancies and cation-cation antisites) are also the dominant defects in other II-IV-V₂ semiconductors, such as ZnGeN_2 , ZnSnN_2 , and ZnSnP_2 [51–55], so it is also natural to focus on these defects in ZnGeP_2 . However, an obvious difference should be noted between ZnGeP_2 and other II-IV-V₂ semiconductors, i.e., ZnGeP_2 has a high density of defects, but also high resistivity, so the defects do not increase the electrical conductivity, in contrast to the cases in other II-IV-V₂ (ZnSnN_2 , ZnSnP_2) semiconductors, which are found to have metalliclike conductivity contributed by a high density of defects [51,52,55–58]. This difference indicates that the defect physics may be quite different in ZnGeP_2 .

Here, we revisit the defect physics of ZnGeP_2 through systematic first-principles calculations based on a hybrid functional and find that the defect physics of ZnGeP_2 is quite unexpected, because a very high density of cation-anion antisite defects (Ge_{P} and P_{Ge}) can form and become the dominant defects. The importance of these cation-anion antisites has been neglected since 1976 and deserves special attention in future defect characterization studies. Furthermore, the high density of antisite defects, including the cation-anion antisites Ge_{P} and P_{Ge} , and cation-cation antisites Ge_{Zn} and Zn_{Ge} , induces serious donor-acceptor compensation, resulting in a low hole carrier density, and thus, high resistivity. The calculated PL spectra of these defects show that the PL peaks around 1.4 and 1.6 eV may originate from Ge_{P} and P_{Ge} , respectively, and the 1.2 eV peak originates from Ge_{Zn} , which challenges the previous opinions that the P vacancies are responsible for the two PL peaks at 1.4 and 1.6 eV.

II. CALCULATION METHODS

A. Defect formation energies

All structural relaxation and total-energy calculations are performed based on density-functional theory and plane-wave pseudopotential methods, as implemented in the Vienna *ab initio* simulation package (VASP) [59]. For the exchange-correlation functional, the hybrid functional in the Heyd-Scuseria-Ernzerhof (HSE) [60,61]

form is adopted with the standard exchange parameter $\alpha = 0.25$ and screening parameter $\mu = 0.2 \text{ \AA}^{-1}$. The projector-augmented-wave (PAW) [62,63] pseudopotentials are used, and Zn $3d^{10} 4s^2$, Ge $4s^2 4p^2$, and P $3s^2 3p^3$ electrons are treated as valence electrons. The energy cutoff of the plane-wave basis is set to 350 eV, and a $6 \times 6 \times 3$ Monkhorst *k*-point mesh [64] is used for the primitive cell and single Γ point for the 144-atom defect supercell. The convergence test with a larger supercell and denser *k*-point meshes shows that the results are converged.

The formation energy of the point defect α in the ionized charge state q is calculated by [65,66]

$$\Delta E_f(\alpha, q) = E(\alpha, q) - E(\text{ZnGeP}_2) + \sum n_i(E_i + \mu_i) + q(E_F + \varepsilon_{\text{VBM}} + \Delta V_{\text{align}}) + E_{\text{image}}, \quad (1)$$

where $E(\alpha, q)$ is the total energy of the supercell with a defect α in its charge state q , and $E(\text{ZnGeP}_2)$ is the total energy of the pure ZnGeP_2 supercell. μ_i is the atomic chemical potential of an atom reservoir of element i , referenced to the energy, E_i , of the pure elemental phases of Zn, Ge, and P. ε_{VBM} is the eigenvalue of the valence-band-maximum (VBM) state in the bulk supercell and E_F is the Fermi energy referenced to the VBM level. ΔV_{align} aligns the averaged electrostatic potential of the farthest area from the defect in the supercell. E_{image} accounts for the spurious interaction caused by the charged defect image and neutralizing background charge [67,68]. The total correction $q\Delta V_{\text{align}} + E_{\text{image}}$ is compared with that calculated with the scheme proposed by Freysoldt *et al.* [69] in the Supplemental Material [70], showing that the transition-level difference is negligible.

B. Defect and carrier densities

For a defect α in its charge state q , the equilibrium density $n(\alpha, q)$ is a function of its formation energy, which can be given by [65,66]

$$n(\alpha, q) = N_{\text{sites}} g_q e^{[-\Delta E_f(\alpha, q)/(k_B T)]}, \quad (2)$$

where $\Delta E_f(\alpha, q)$ is the defect formation energy, k_B is the Boltzmann constant, and T is the temperature. N_{sites} is the number of defect sites per unit volume, and g_q is the degeneracy factor, which reflects the number of possible configurations for electrons occupying the defect level and changes with the charge state q .

Since the ionized defects produce carriers and become charged, we can calculate the charge density of all ionized acceptor defects (N_A^-) and the charge density of all ionized donor defects (N_D^+). For nondegenerate semiconductors, the density of hole and electron carriers follows

the Boltzmann distribution, which is given by

$$p_0 = N_v e^{-E_F/k_B T}, \quad (3)$$

$$n_0 = N_c e^{(E_F - E_g)/k_B T}, \quad (4)$$

where N_v and N_c are the effective density of states for the valence-band and conduction-band edges, respectively. N_A^- , N_D^+ , n_0 , and p_0 should satisfy the charge-neutrality condition

$$p_0 + N_D^+ = n_0 + N_A^-. \quad (5)$$

By solving Eq. (5) self-consistently, we can determine the Fermi level, E_F ; electron and hole carrier density; and the density of all point defects in different charge states under different chemical-potential (growth) conditions [71,72].

Since the crystals are usually grown at a high growth temperature and then annealed to room temperature, defects form during growth and may change their charge states after annealing, which can change the Fermi level and carrier density. Therefore, we determine the density of defects at room temperature through two-step calculations [66,73,74]. In the first step, we solve Eq. (5) at a high growth temperature and determine the density of all defects in different charge states, from which we can determine the total density of each defect (summed density of the defect at all possible charge states). In the second step, we fix the total density of each defect to that determined in the first step and redistribute the density at different charge states, according to the Fermi-Dirac distribution of electrons on the defect levels at room temperature (here the Fermi level is determined through solving the charge-neutrality Eq. (5) at room temperature). With the redistributed density of defects at different charge states and the Fermi level, the carrier density at room temperature can also be calculated.

C. Photoluminescence spectrum

The calculation of the photoluminescence line shape is according to the absolute luminescence intensity as a function of photon energy $\hbar\omega$ given by [75,76]

$$I(\hbar\omega) = \frac{e^2 n_r \omega^3}{3m_e^2 \varepsilon_0 \pi c^3 \hbar} \sum_m p_m \sum_n |\langle \Psi_{im} | \hat{p} | \Psi_{fn} \rangle|^2 \delta(E_{ZPL} + E_{im} - E_{fn} - \hbar\omega), \quad (6)$$

where e is the elementary charge, n_r is the index of refraction, m_e is the mass of an electron, ε_0 is the vacuum permittivity, and c is the speed of light. p_m is the Boltzmann factor, which reflects the thermal occupation of the

initial vibrational state m . Ψ_{im} and Ψ_{fn} are the total (electron + nuclear) wave functions for the initial state (indexed by m) and final state (indexed by n). \hat{p} is the momentum operator. Using the Condon approximation, which assumes that the momentum matrix element $M_{if} = \langle \psi_i | \hat{p} | \psi_f \rangle$ is independent of the nuclear configuration, the luminescence intensity can be rewritten as

$$I(\hbar\omega) = N \omega^3 f(\hbar\omega), \quad (7)$$

where $N = [(e^2 n_r) / (3m_e^2 \varepsilon_0 \pi c^3 \hbar)] |M_{if}|^2$ contains the parameters independent of the photon energy $\hbar\omega$. Since the luminescence intensity will be normalized, the exact calculation of N can be replaced by a normalization factor $f(\hbar\omega)$ is the so-called spectral function, which can be written as [77–79]

$$f(\hbar\omega) = \sum_m p_m \sum_n |\langle \chi_{im} | \chi_{fn} \rangle|^2 \delta(E_{ZPL} + E_{im} - E_{fn} - \hbar\omega), \quad (8)$$

where $\langle \chi_{im} | \chi_{fn} \rangle$ is the overlap integral for initial and final vibrational wave functions, and E_{im} and E_{fn} are the corresponding phonon energies, which can be numerically evaluated by solving the one-dimensional (1D) Schrödinger equation along the 1D-harmonic potential-energy surface for initial and final states. The δ function ensures energy conservation that the transition from Ψ_{im} to Ψ_{fn} is allowed only when the sum of the electronic energy difference E_{ZPL} (E_{ZPL} is the energy of zero-phonon line corresponding to the charge-state transition level calculated for defects) and vibrational energy difference $E_{im} - E_{fn}$ equals the emitted photon energy $\hbar\omega$. Since the energies of phonon states are discrete, with a quantized energy difference under the assumption of harmonic vibration, the δ function should be broadened to produce a continuous luminescence spectrum. Here, we replace the δ function by a Gaussian, as suggested by Alkauskas *et al.* [78].

III. RESULTS AND DISCUSSION

A. Phase stability

To calculate the formation energies of defects according to Eq. (1), we need to determine the chemical potentials of Zn, Ge, and P that can stabilize the ternary compound ZnGeP₂. ZnGeP₂ has a tetragonal chalcopyrite structure with the space group of $I-42d$, which can be derived from the zinc blende structure by orderly occupation of the cation sites with Zn and Ge [shown in Fig. 1(a)]. Our HSE-calculated lattice constants, $a = 5.468 \text{ \AA}$ and $c = 10.745 \text{ \AA}$, are highly consistent with experimental values, as shown in Table I. In contrast, the semilocal generalized-gradient approximation (GGA) functional [85] overestimates the lattice constants, while local-density approximation (LDA)

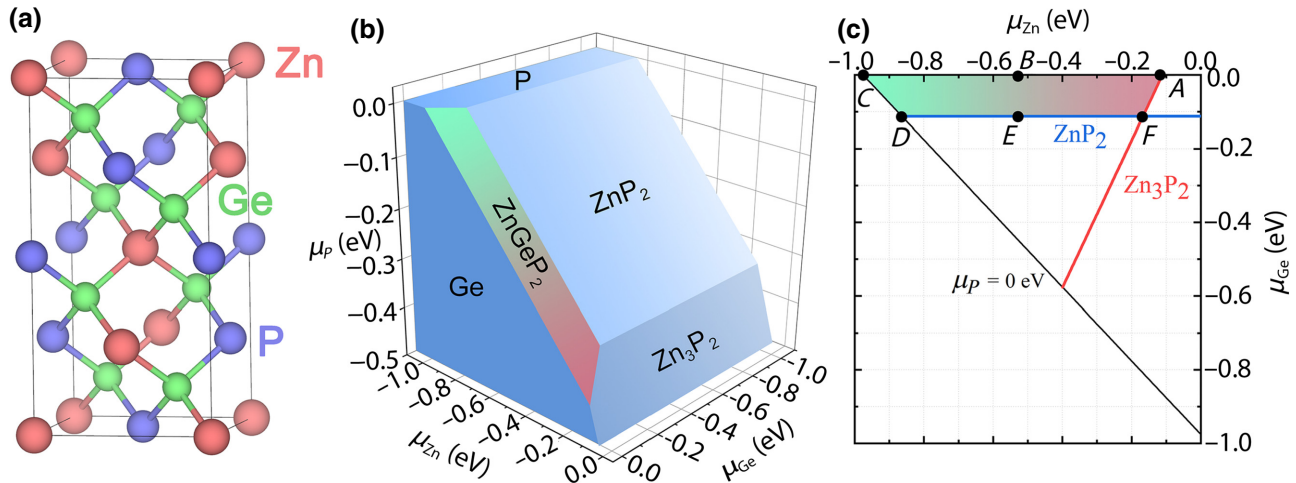


FIG. 1. (a) Unit cell of chalcopyrite ZnGeP₂ crystal structure. (b) Thermodynamic chemical-potential region (shown in gradient color) stabilizing ZnGeP₂ with respect to competing secondary phases, such as Zn, Ge, P, Zn₃P₂, and Zn₂P₂ in three-dimensional (μ_{Zn} , μ_{Ge} , μ_{P}) space. (c) Projection of the chemical-potential region on the (μ_{Zn} , μ_{Ge}) plane. Six points A, B, C, D, E, and F are selected as the synthesis conditions under which the defect properties will be calculated.

[86] underestimates them. With the HSE-optimized structure, the band gap of ZnGeP₂ is found to be 2.058 eV at the Γ point, which also agrees well with the experimental values (2.0–2.1 eV) [22,87,88] and a recent HSE-calculated value of 2.15 eV [89].

When this ternary compound ZnGeP₂ is stable, relative to the competing phases that can be formed by the three elements Zn, Ge, and P, the ranges of their chemical potentials, μ_i ($i = \text{Zn}, \text{Ge}, \text{or P}$), should be limited. Under the thermodynamic equilibrium, the chemical potentials of Zn, Ge, and P should satisfy

$$\mu_{\text{Zn}} + \mu_{\text{Ge}} + 2\mu_{\text{P}} = \Delta E_f(\text{ZnGeP}_2),$$

where $\Delta E_f(\text{ZnGeP}_2) = -0.98$ eV is the calculated formation energy of ZnGeP₂ and is slightly lower than the GGA-calculated value of -0.89 eV [90]. Because $\mu_i = 0$ means the element is so rich that its pure elemental phase can form, $\mu_{\text{Zn}} < 0$, $\mu_{\text{Ge}} < 0$, and $\mu_{\text{P}} < 0$ should also be satisfied in order to ensure that no elemental phases of Zn, Ge, or P coexist in the synthesized samples. In order to avoid the coexistence of secondary phases, such as Zn₃P₂

TABLE I. Calculated lattice constants of ZnGeP₂, compared with experimental and previously calculated results.

	a (Å)	c (Å)	$\eta = c/2a$
This work	5.468	10.745	0.983
Experiments	5.46 [35]	10.71 [35]	0.981
	5.466 [80]	10.722 [80]	0.981
	5.465 [81]	10.771 [81]	0.985
Calculations	5.499 [82]	10.840 [82]	0.986 (GGA)
	5.396 [83]	10.665 [83]	0.988 (LDA)
	5.473 [84]	10.749 [84]	0.982 (HSE)

and Zn₃P₂, the chemical potentials should also satisfy

$$3\mu_{\text{Zn}} + 2\mu_{\text{P}} < \Delta E_f(\text{Zn}_3\text{P}_2),$$

$$\mu_{\text{Zn}} + 2\mu_{\text{P}} < \Delta E_f(\text{ZnP}_2),$$

where $\Delta E_f(\text{Zn}_3\text{P}_2) = -1.20$ eV and $\Delta E_f(\text{ZnP}_2) = -0.86$ eV are the calculated formation energies of Zn₃P₂ and ZnP₂, respectively. Based on the above equations and inequations, we can determine the chemical-potential region that stabilizes pure ZnGeP₂, which is plotted with gradient color in Fig. 1(b) [in three-dimensional (μ_{Zn} , μ_{Ge} , μ_{P}) space] and Fig. 1(c) [projected on the two-dimensional (μ_{Zn} , μ_{Ge}) plane]. As μ_{Ge} becomes lower, and thus, Ge becomes poorer under the synthesis conditions, Zn₃P₂ and ZnP₂ will form. Therefore, μ_{Ge} is restricted to a small range near 0 eV, meaning that the Ge-rich condition should always be satisfied for synthesizing pure ZnGeP₂ samples. It should be noted that there are differences between the calculated and experimental formation energies of compounds, e.g., the calculated values of GaN, Zn₃P₂, and ZnP₂ are -1.34 , -1.20 , and -0.86 eV, respectively, while the experimental values are -1.63 , -1.65 , and -1.26 eV, respectively [91–94]. The difference is due to the error in the elemental-phase reference energies [92], which is common in defect calculations of compound semiconductors [95] and can cause an error of around 0.2–0.3 eV in the elemental chemical potential and defect-formation energies.

It should also be noted that the stable chemical-potential range of ZnGeP₂ had also been calculated by Jiang *et al.* [43,44]; however, their results differ significantly from ours. We attribute the difference to three reasons: (i) they do not consider an important secondary phase, ZnP₂,

which can limit the stable chemical-potential region significantly; (ii) they consider a secondary phase, GeP, which, however, is found to be intrinsically unstable with a positive formation energy, according to our hybrid functional calculations, and thus, does not influence the chemical-potential region, and (iii) they use the semilocal LDA functional, but we use the hybrid functional. The first reason is major, because our test calculations show that the stable region calculated using different functionals (as shown in Fig. S1 within the Supplemental material [70]) are all consistent and similar to that in Fig. 1 as far as ZnP₂ is considered. Our results are also consistent with recent

x-ray photoelectron spectroscopy results that the impurity phases during ZnGeP₂ growth are Zn₃P₂ and ZnP₂ [96].

B. Dominant point defects

After determining the stable chemical-potential region of ZnGeP₂, we select six representative points in the region and calculate the defect properties in the ZnGeP₂ samples synthesized under these conditions. In Fig. 2, the formation energies of all point defects (including three vacancies, V_{Zn}, V_{Ge}, and V_P; six antisites, Zn_{Ge}, Zn_P, Ge_{Zn}, Ge_P, P_{Zn}, and P_{Ge}; and three interstitials Zn_i, Ge_i, and P_i) in different

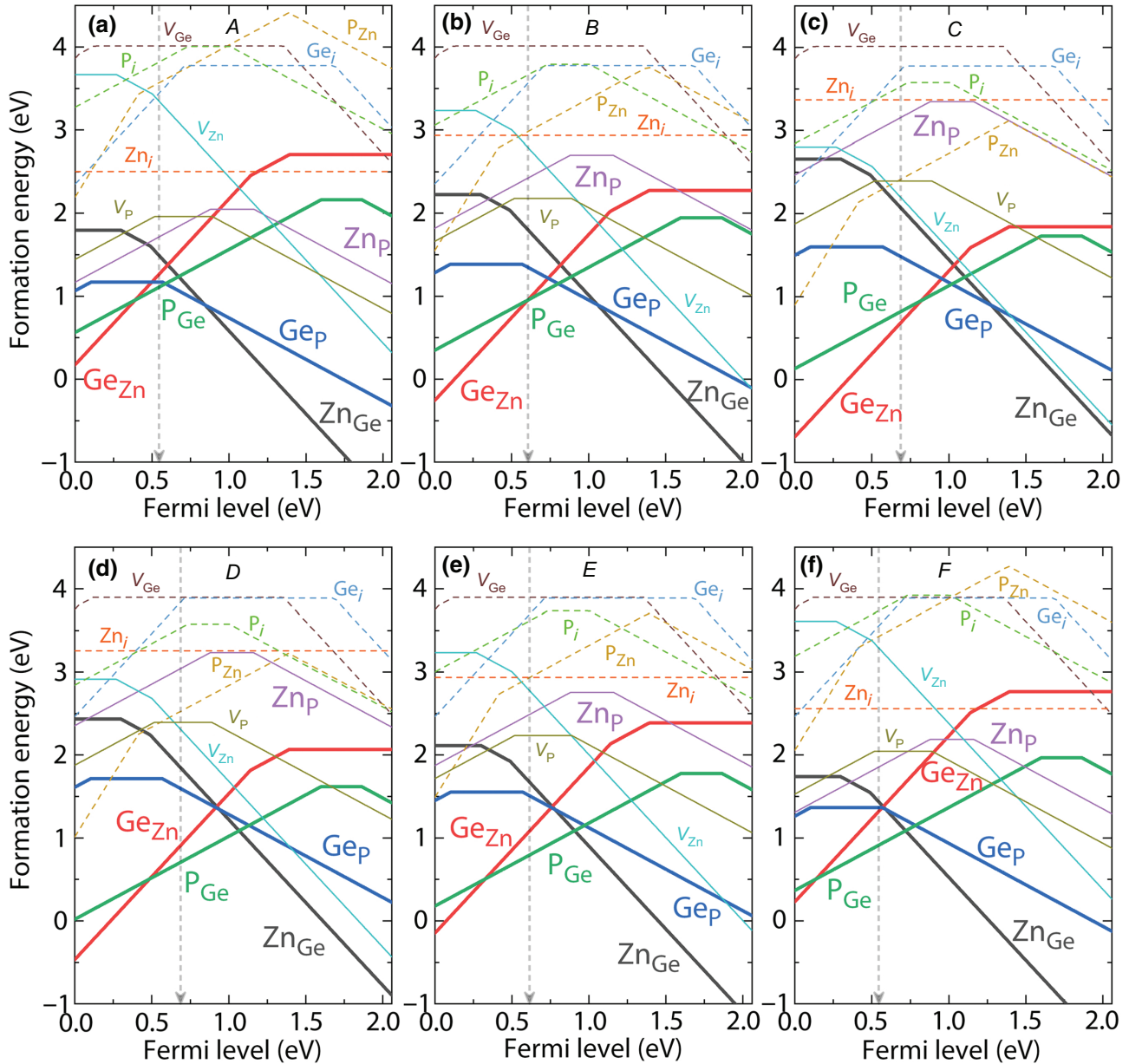


FIG. 2. Calculated formation energies of point defects in different charge states as a function of Fermi level under the chemical-potential points (a) A, (b) B, (c) C, (d) D, (e) E, and (f) F shown in Fig. 1. Gray arrows denote the Fermi levels under the corresponding chemical-potential conditions (calculated in Fig. 5).

charge states are plotted as functions of the Fermi level. For the three interstitials, we consider at least 30 interstitial sites from which we search for the low-energy configurations after performing calculations for all sites. Figure 2 shows the formation energies of the lowest-energy configurations, which are always higher than 2 eV, so their density should be very low (for other higher-energy configurations, their density should be even lower, so they are not shown in Fig. 2). The atomic structures of the lowest-energy interstitial configurations are shown in Fig. S2 within the Supplemental Material [70].

Among the defects, V_{Ge} , P_{Zn} , and all interstitial defects have too-high formation energies (always higher than 1 eV, as shown by the dashed lines), so they have negligible density in the synthesized samples and are thus unimportant. Four antisite defects, including two cation-anion antisites, Ge_P and P_{Ge} , and two cation-cation antisites, Ge_{Zn} and Zn_{Ge} , are found to be the dominant defects with low formation energies under the six representative synthesis conditions. Ge_{Zn} and P_{Ge} can be positively charged (produce electron carriers) and have the lowest formation energies in the *p*-type samples with the Fermi level close to the VBM level, while Zn_{Ge} and Ge_P can be negatively charged (produce hole carriers) and have the lowest formation energies in the *n*-type samples with the Fermi level close to the conduction-band-minimum (CBM) level. Therefore, they should have important influences on the electrical and optical properties of ZnGeP_2 . We will now discuss their properties individually.

Ge_{Zn} acts as a deep donor with its $(0/+)$ and $(+/2+)$ transition levels located at 0.66 and 0.92 eV below the CBM level, as shown in Fig. 3. It is in the +1 and +2 charge states when the Fermi level ranges from 0 to 1.39 eV, indicating that it becomes electrically active and contributes to *n*-type conductivity in this Fermi-level range. Setzler *et al.* [17,18] observed the existence of singly ionized Ge_{Zn} (+1 charge state) using EPR, consistent with our calculated low formation energy and high

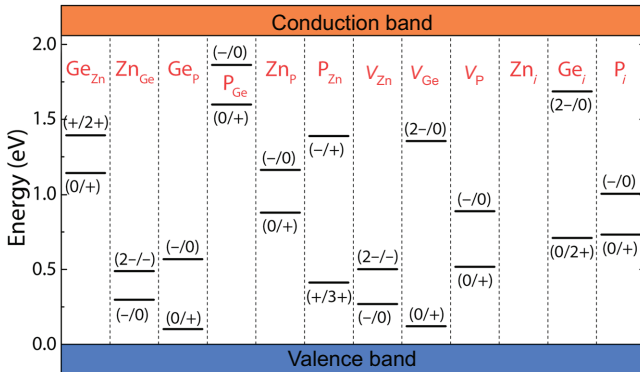


FIG. 3. Calculated charge-state transition levels of point defects in the band gap of ZnGeP_2 .

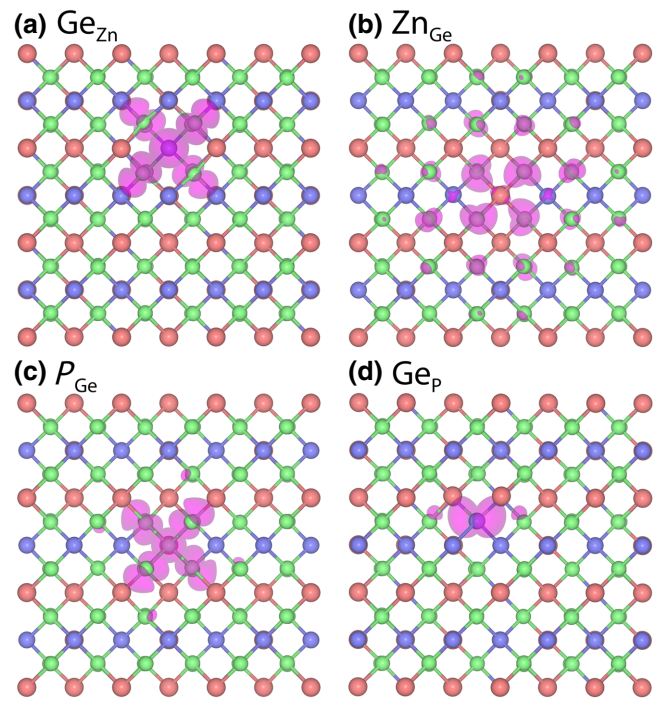


FIG. 4. Norm-squared wave function of the defect eigenstates produced by (a) Ge_{Zn} , (b) Zn_{Ge} , (c) P_{Ge} , and (d) Ge_P in their neutral states. Isovalues of isosurfaces are set to 20% of the maximum. Colors of Zn, Ge, and P atoms are the same as those in Fig. 1.

density of Ge_{Zn} in *p*-type samples. However, according to our calculated results, the formation energy of $\text{Ge}_{\text{Zn}}^{2+}$ is much lower than that of Ge_{Zn}^+ , when the Fermi level is low, so we predict that a higher density of $\text{Ge}_{\text{Zn}}^{2+}$ should also exist in *p*-type ZnGeP_2 . Significant atomic relaxation around Ge_{Zn} is found when the charge state changes from the neutral (0) state to the ionized +1 and +2 states. The four neighboring P atoms undergo an inward relaxation by 4.1% and 6.9% in the +1 and +2 charge states, respectively. The deep nature of the Ge_{Zn}^+ ($0/+$) and $(+/2+)$ donor states and the large structural relaxation during ionization can be understood according to electronic component analysis of the donor states. In Fig. 4(a), we plot the norm-squared wave function of the donor state. Obviously, the wave function is mainly localized on the Ge cation and its neighboring P anions, which is the antibonding state of Ge 4s and P 3p hybridization. Because the Ge 4s orbital level is much lower than that of the Zn 3s level, the donor level is low and deep in the band gap. In the neutral state, the antibonding donor level is occupied, so the Ge – P bond lengths are large; however, the level becomes partially occupied when the defect is ionized into the +1 state and fully unoccupied when it is ionized into the +2 state, so the Ge – P bonds shorten significantly.

In contrast to Ge_{Zn} , Zn_{Ge} is an acceptor with relatively shallow $(-/0)$ and $(2-/-)$ transition levels, located at 0.30 and 0.49 eV, above the VBM level. When

the Fermi level is close to the CBM, ionized Zn_{Ge}^{2-} can have a very low formation energy and high density, which can limit the *n*-type conductivity. Atomic relaxation during Zn_{Ge} ionization is rather small, i.e., the corresponding $Zn - P$ bonds in the $Zn_{Ge} - 1$ and -2 states remain almost unchanged. Since the $Zn_{Ge} (-/0)$ and $(2/-)$ acceptor levels are relatively shallow, the wave function of the acceptor state is more delocalized, as shown in Fig. 4(b), and the state is mainly composed of the $P\ 3p$ orbitals.

P_{Ge} is an amphoteric defect that can both be positively charged (ionized donor) and negatively charged (ionized acceptor). It has the $(0/+)$ transition level at 0.46 eV below the CBM and the $(-/0)$ level at 0.20 eV below the CBM. Figure 4(d) shows the wave function of the $P_{Ge}\ (0/+)$ donor level. Interestingly, the wave function is very similar to that of the Ge_{Zn} donor level and localized mainly around the antisite P and surrounding P atoms, which indicates that the donor state is the antibonding state of hybridization between $P\ 3s$ and the surrounding $P\ 3p$ orbitals. This finding is in good agreement with the EPR-measured hyperfine interaction for P_{Ge}^0 , which shows that the spin density is localized on a central phosphorus and four equivalent neighboring phosphorus atoms [48]. The donor level of P_{Ge} is higher in energy than that of Ge_{Zn} . The reason is twofold: (i) the $P\ 3s$ orbital energy is higher than the $Ge\ 4s$ orbital energy; and (ii) the $P-P$ bond around P_{Ge} is shorter than the $Ge-P$ bond around Ge_{Zn} by 11.5% in the neutral state and by 10.0% in the $+1$ charge state, indicating that the $P-P\ s-p$ hybridization around P_{Ge} is stronger than the $Ge-P\ s-p$ hybridization around Ge_{Zn} , and thus, pushes the antibonding donor level upward.

Although Ge_p is also amphoteric, it is the opposite of P_{Ge} , which stays in the -1 charge state over a wide range of Fermi levels, but becomes the $+1$ charge state only when the Fermi level is very low and close to the VBM level. The wave function in Fig. 4(c) shows that the $Ge_p\ (-/0)$ acceptor state is quite different from other defect states, i.e., although it is localized around the defect site, it has little hybridization contribution from the surrounding Ge around the antisite Ge . The state is mainly the $Ge\ 4p$ orbital and has a little contribution from the second-nearest-neighbor $P\ 3p$ orbitals. Since hybridization with the neighboring atoms is very weak, $Ge_p\ (-/0)$ acceptor state can be viewed as a nonbonding state of the $Ge\ 4p$ orbital.

C. Defect and carrier density

Figure 5 plots the calculated density of all defects in different charge states, Fermi energies, and hole-carrier density changes with the chemical-potential points from *A* to *F*. Obviously, the four antisite defects in different charge states have much higher density (as high as $10^{17}-10^{18}\ cm^{-3}$) than those of other defects, indicating that

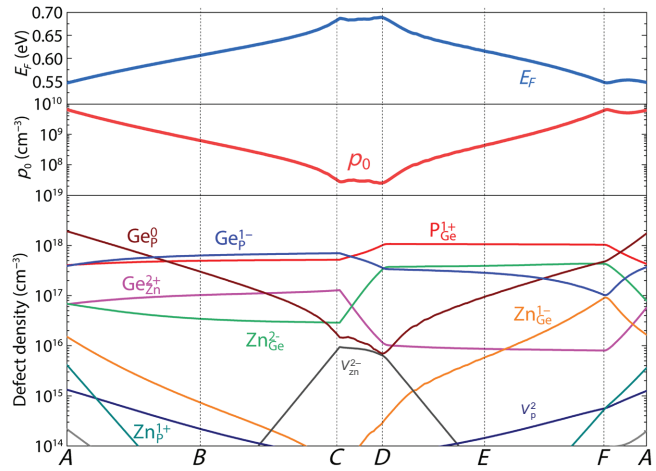


FIG. 5. Calculated density of all defects, Fermi levels, and hole-carrier density at room temperature (300 K) in $ZnGeP_2$ crystals grown at a high temperature (1300 K) and under different chemical conditions (corresponding to the chemical-potential points from *A* to *F* in Fig. 1). Since the allowed range of μ_{Ge} is narrow in Fig. 1, its influence on the results is small, and thus, the differences between *A* and *F*, *B* and *E*, or *C* and *D* points are not large.

they are indeed the dominant defects in this ternary compound $ZnGeP_2$. Besides the four antisites, V_P , V_{Zn} , and Zn_P can also have a density higher than $10^{14}\ cm^{-3}$, so they may also have important influences on the electrical and optical properties of $ZnGeP_2$.

One abnormal character of $ZnGeP_2$ defect properties is the high density of anion-cation antisite defects Ge_p and P_{Ge} . In conventional III-V and II-VI semiconductors, such as GaAs [97], GaN [98], InP [99], or ZnO [100], the anion-cation antisite defects usually do not exist, i.e., their density is negligible. Furthermore, in other II-IV-V₂ ternary compounds, such as $ZnSnN_2$ [51,52], $ZnGeN_2$ [53,54], and $ZnSnP_2$ [55], that have been studied in the past decade, the anion-cation antisite defects have never been reported to have a high density ($Zn-Sn$ and $Zn-Ge$ antisites are found to be the only dominant defects in $ZnSnN_2$, $ZnGeN_2$, and $ZnSnP_2$, but Sn-N, Ge-N, or Sn-P antisites have not been reported). However, our calculations show that Ge_p and P_{Ge} can have a high density in chalcopyrite-structured $ZnGeP_2$. The origin can be attributed to the small atomic size difference and the small electronegativity difference between Ge and P , compared with those of Sn-N, Sn-P, and Ge-N. It should be noted that the anion-cation antisite defects, Ge_p and P_{Ge} , had not been considered by Jiang *et al.* in their calculation study on the defect properties of $ZnGeP_2$ [43,44], so their high density had never been reported.

Although Ge_p and P_{Ge} have high densities in $ZnGeP_2$, their compensation limits the carrier density and electrical conductivity to a low level. As shown in Figs. 2 and 5,

the compensation between Ge_P^- and P_{Ge}^+ pins the Fermi level at 0.55 eV at point *A* (under Zn-rich conditions) and at 0.69 eV at point *C* (under Zn-poor conditions), so the corresponding hole-carrier density is always low, only 6.4×10^9 and $2.5 \times 10^7 \text{ cm}^{-3}$, respectively. Under Zn-rich conditions, the calculated hole density of $6.4 \times 10^9 \text{ cm}^{-3}$ is in good agreement with the experimentally measured value of about 10^{10} cm^{-3} in *p*-type $ZnGeP_2$ [31]. Under Zn-poor and Ge-poor conditions, the hole density becomes even lower, which also agrees with the high resistivity observed in $ZnGeP_2$ grown by HPVT [19]. Experimentally, the HPVT samples are reported to be *n*-type, but with high resistivity [19]; however, the low carrier density predicted by our calculations and the Fermi level at the middle of the band gap indicate that the HPVT samples are actually intrinsic (rather than *n*-type, just more *n*-type and less *p*-type than the Bridgman-grown samples), and thus, have high resistivity. The experiments also show that the density of both the donor and acceptor defects are around 10^{19} cm^{-3} [26,27], which are close to our calculated density of the dominant cation-anion antisites P_{Ge} and Ge_P . Both our calculations and previous experiments show a high density of donor and acceptor defects, but low density of hole carriers, confirming that there is serious donor-acceptor compensation in $ZnGeP_2$.

Despite the predicted high density, four of the dominant defects in the ionized charge states, e.g., Ge_P^- , P_{Ge}^+ , Ge_{Zn}^{2+} , and Zn_{Ge}^{2-} , are not identified by experiments. This is possibly because the characterization of defects in $ZnGeP_2$ is mostly through EPR in past decades, but, for the four charged defects, the defect levels are always fully occupied or empty (full-shell state), which do not have unpaired electrons, and thus, cannot be observed by EPR. Therefore, the EPR characterization reports only P_{Ge}^0 , Ge_{Zn}^+ , and Zn_{Ge}^- [17,35,48], which have lower densities than those of Ge_P^- , P_{Ge}^+ , Ge_{Zn}^{2+} , and Zn_{Ge}^{2-} , according to our calculation in Fig. 5. Considering the much higher density of ionized defects that are not observed in EPR characterization, we call for a characterization study of defects in $ZnGeP_2$ using other techniques.

D. Defect origin of photoluminescence peaks

A series of experiments show that the *p*-type Bridgman-grown $ZnGeP_2$ have PL peaks at around 1.23 [40], 1.4 [23,41], and 1.6 eV [20,23,41], while the HPVT-grown samples have only the 1.2 eV peak [19]. In the literature, the 1.4 and 1.6 eV peaks are both attributed to the defect V_P [23,41], while the 1.2 eV defect is attributed to the antisite defect on the cation site [19]. According to our calculated defect density, V_P has a much lower density than that of the four dominant antisite defects, Ge_{Zn} , Zn_{Ge} , Ge_P , and P_{Ge} . It is thus natural to investigate if the four antisites produce any PL peaks and if they are responsible for the three peaks observed experimentally.

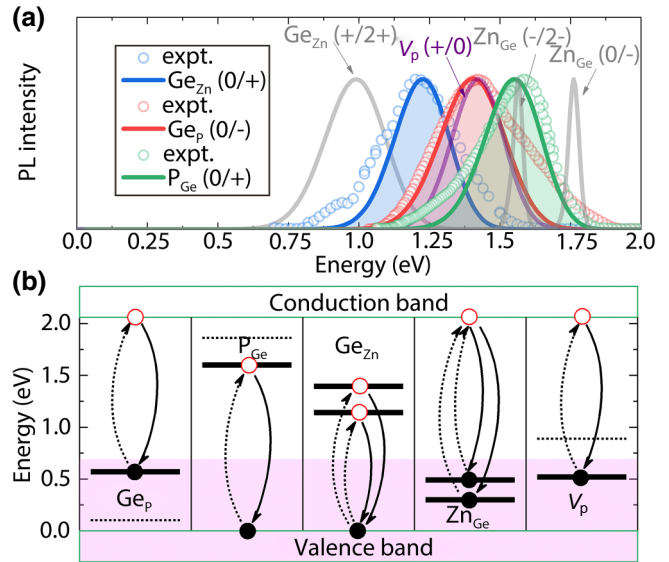


FIG. 6. (a) Calculated photoluminescence spectrum of Ge_P , P_{Ge} , Zn_{Ge} , Ge_{Zn} , and V_P in comparison with experimental data extracted from Refs. [19,23,41]. Solid lines are calculated results and dots are experimental values. Spectral peaks are normalized. (b) Corresponding schematic band diagram of carrier excitation and recombination processes. Fermi level is set to 0.69 eV in the shaded pink area.

Since the Fermi level is located at 0.55–0.69 eV above the VBM, V_P , Ge_P , and Zn_{Ge} are in the neutral and negatively charged states, so their defect levels are occupied by electrons [Fig. 6(b)], which can be excited to the CBM level and produce photoluminescence when the excited electron at the CBM level has a radiative transition back to the defect level. The defect levels of V_P , Ge_P , and Zn_{Ge} are 1.2–2 eV lower than the CBM level, so their emissions can be possible origins of the 1.2, 1.4, and 1.6 eV PL peaks. The levels of Ge_{Zn} and P_{Ge} are high (1.2–1.8 eV above VBM), so they are unoccupied [Fig. 6(b)], and the two defects are in the positively charged states. Under photon illumination, the electrons in the VBM level can be excited to these high levels, then a hole is produced at the VBM level, and the defect Ge_{Zn} (P_{Ge}) changes its charge state from positive to neutral. The radiative transition from the defect level to the VBM level can give rise to emissions in the range of 1.2–1.8 eV, so they can also be possible origins of the 1.2, 1.4, and 1.6 eV PL peaks.

Figure 6(a) shows the calculated PL spectra of possible origin defects, according to the spectral function [78], and the critical factors influencing the spectra are shown in Table II. In the Supplemental Material [70], we also show the detailed one-dimensional configuration coordinate diagram for each defect, which illustrates the corresponding electron excitation and recombination processes. Interestingly, the PL spectra of three defects, Ge_{Zn} , Ge_P , and

TABLE II. Calculated factors that determine the PL spectra, according to the one-dimensional configuration coordinate diagram.

Defect	ΔQ (amu $^{1/2}$ Å)	E_{emission} (eV)	$\hbar\Omega_g$ (meV)	E_{rel} (eV)	S_g
Ge _{Zn} (0/+)	1.48	1.23	26.79	0.154	5.74
Ge _{Zn} (+/2+)	1.28	0.98	29.42	0.159	5.42
Ge _P (0/-)	1.72	1.37	22.08	0.174	7.87
P _{Ge} (0/+)	1.19	1.55	31.15	0.125	4.01
V _P (+/0)	2.64	1.40	14.55	0.141	9.69
Zn _{Ge} (0/-)	0.34	1.76	23.95	0.004	0.15
Zn _{Ge} (-/2-)	0.42	1.56	18.19	0.007	0.37

ΔQ , structural difference in generalized coordinate; E_{emission} , emission energy that corresponds to the PL peak; $\hbar\Omega_g$, effective ground-state vibrational energy fitted by our first-principles calculation data; E_{rel} , lattice relaxation energy; S_g , ground-state Huang-Rhys factor.

P_{Ge} , are highly consistent with the line shapes of the experimental spectra.

For Ge_P, photoexcitation changes its state from Ge_P^- to Ge_P^0 (with an electron in the CBM level), and then the transition from Ge_P^0 to Ge_P^- gives rise to a PL peak at 1.37 eV, so it can be the origin of the 1.4 eV PL peak observed experimentally [23,41]. For P_{Ge}, the photoexcitation changes its state from P_{Ge}^+ to P_{Ge}^0 (with a hole in the VBM level), and the transition from P_{Ge}^0 to P_{Ge}^+ gives rise to a PL peak at 1.55 eV, which can be origin of the observed 1.6 eV PL peak [20,23,41]. The calculated PL line shapes of these two defects both agree well with the measured PL spectra. Especially, both experiments and calculations show that the 1.37 eV emission has a broader band than that of the 1.55 eV emission, which can be ascribed to stronger electron-phonon coupling, as reflected by the larger Huang-Rhys factors (see Table II). For Ge_{Zn}, the ground state is the positively charged state, Ge_{Zn}^+ , and the photoexcited state is Ge_{Zn}^0 with a hole in the VBM level. The transition from Ge_{Zn}^0 to Ge_{Zn}^+ gives rise to a 1.23 eV PL peak, which can be the origin of the PL peak at 1.2 eV [19].

The attribution of the PL origin to antisite Zn_{Ge} can be easily ruled out because either the (0/-) or (-/2-) transition shows a very narrow PL shape, in contrast to the experimental one. This is in accordance with the small Huang-Rhys factors (weak electron-phonon coupling) shown in Table I. V_P was previously assumed to be the source of the PL peaks at 1.4 and 1.6 eV. Our calculation also indicates it has a similar emission energy of 1.40 eV and large electron-phonon coupling. However, according to Fig. 6(a), V_P shows a narrower PL than that of Ge_P, and the shape of Ge_P agrees with the experimental result better. The smaller full width at half maximum of V_P PL can be ascribed to its smaller effective vibrational energy, Ω_g , leading to smaller vibrational wave-function overlap. Considering the higher density of Ge_P than that of V_P, it is reasonable to attribute the origin of the 1.4 eV PL peak to Ge_P, instead of the previously assumed V_P.

The appearance of the defect-induced PL peaks indicates that the defects can also induce obvious optical absorption in the energy range 1–2 eV, which can limit the transparency, and thus, the development of high-power optical devices, such as OPO and SHG devices. Since the densities of these origin defects are high and cannot be diminished to a low level at a high growth temperature of 1300 K through changing the chemical-potential conditions, as shown in Fig. 5, suppressing their optical absorption should be challenging and important in the future development of high-power ZnGeP₂-based optical devices. On the other hand, there may be impurities, such as C, H, and O, introduced during the crystal growth, and how these impurities interact with the intrinsic defects and influence the properties also deserves future study.

IV. CONCLUSIONS

Using first-principles calculations based on a hybrid functional, we find that the defect physics of ZnGeP₂ is quite abnormal compared with other group II-IV-V₂ semiconductors. The anion-cation antisite defects, Ge_P and P_{Ge}, have unexpectedly high density and become the dominant defects in ZnGeP₂. However, their importance has been neglected in long-term studies on the defects in ZnGeP₂ after P_{Ge} was initially discussed in 1976. The calculated PL spectra of Ge_P and P_{Ge} agree well with the experimentally observed PL peaks at 1.4 and 1.6 eV, respectively, indicating that they may be the origin defects of these two PL peaks, which challenges the previous assumptions that V_P is the origin of the two peaks in PL and EPR characterization studies. Both cation-cation (Ge_{Zn}, Zn_{Ge}) and cation-anion (Ge_P, P_{Ge}) antisites are found to have high density, but P_{Ge} and Ge_{Zn} can act as donors, while Ge_P and Zn_{Ge} can act as acceptors, so they cause serious donor-acceptor compensation, which results in a low carrier density and makes the Fermi level of 0.55–0.69 eV above the VBM. The serious donor-acceptor compensation explains the experimentally observed coexistence of both a high density of point defects and high resistance. According to these results, we call for more defect characterization

studies on ZnGeP₂ using experimental techniques besides PL and EPR and highlight the challenge in suppressing the defect-induced optical absorption for developing high-power ZnGeP₂-based optical devices.

ACKNOWLEDGMENTS

This work is supported by the National Natural Science Foundation of China (NSFC) under Grants No. 61722402 and No. 91833302, Shanghai Academic/Technology Research Leader (Grant No. 19XD1421300), the Program for Professor of Special Appointment (Eastern Scholar), the Fok Ying Tung Education Foundation (Grant No. 161060), and the Fundamental Research Funds for the Central Universities.

M. Huang and S. Wang contributed equally to this work.

-
- [1] T. H. Allik, S. Chandra, D. M. Rines, P. G. Schunemann, J. A. Hutchinson, and R. Utano, Tunable 7–12-μm optical parametric oscillator using a Cr,Er:YSGG laser to pump CdSe and ZnGeP₂ crystals, *Opt. Lett.* **22**, 597 (1997).
 - [2] P. B. Phua, K. S. Lai, R. F. Wu, and T. C. Chong, High-efficiency mid-infrared ZnGeP₂ optical parametric oscillator in a multimode-pumped tandem optical parametric oscillator, *Appl. Opt.* **38**, 563 (1999).
 - [3] K. L. Vodopyanov, F. Ganikhannov, J. P. Maffetone, I. Zwieback, and W. Ruderman, ZnGeP₂ optical parametric oscillator with 3.8–12.4-μm tunability, *Opt. Lett.* **25**, 841 (2000).
 - [4] S. Das, G. C. Bhar, S. Gangopadhyay, and C. Ghosh, Linear and nonlinear optical properties of ZnGeP₂ crystal for infrared laser device applications: Revisited, *Appl. Opt.* **42**, 4335 (2003).
 - [5] A. A. Ionin, J. Guo, L. M. Zhang, J. J. Xie, Y. M. Andreev, I. O. Kinyaevsky, Y. M. Klimachev, A. Y. Kozlov, A. A. Kotkov, G. V. Lanskii, A. N. Morozov, V. V. Zuev, A. Y. Gerasimov, and S. M. Grigoryants, Mode-locked CO laser frequency doubling in ZnGeP₂ with 25% efficiency, *Laser Phys. Lett.* **8**, 723 (2011).
 - [6] M. W. Haakestad, H. Fonnum, and E. Lippert, Mid-infrared source with 0.2 J pulse energy based on nonlinear conversion of Q-switched pulses in ZnGeP₂, *Opt. Express* **22**, 8556 (2014).
 - [7] M. Gebhardt, C. Gaida, P. Kadwani, A. Sincore, N. Gehlich, C. Jeon, L. Shah, and M. Richardson, High peak-power mid-infrared ZnGeP₂ optical parametric oscillator pumped by a Tm:fiber master oscillator power amplifier system, *Opt. Lett.* **39**, 1212 (2014).
 - [8] Z. Lei, C. Zhu, C. Xu, B. Yao, and C. Yang, Growth of crack-free ZnGeP₂ large single crystals for high-power mid-infrared OPO applications, *J. Cryst. Growth* **389**, 23 (2014).
 - [9] B. Q. Yao, Y. J. Shen, X. M. Duan, T. Y. Dai, Y. L. Ju, and Y. Z. Wang, A 41-W ZnGeP₂ optical parametric oscillator pumped by a Q-switched Ho:YAG laser, *Opt. Lett.* **39**, 6589 (2014).
 - [10] S. Wandel, M.-W. Lin, Y. Yin, G. Xu, and I. Jovanovic, Parametric generation and characterization of femtosecond mid-infrared pulses in ZnGeP₂, *Opt. Express* **24**, 5287 (2016).
 - [11] T. Kanai, P. Malevich, S. S. Kangaparambil, K. Ishida, M. Mizui, K. Yamanouchi, H. Hoogland, R. Holzwarth, A. Pugzlys, and A. Baltuska, Parametric amplification of 100 fs mid-infrared pulses in ZnGeP₂ driven by a Ho:YAG chirped-pulse amplifier, *Opt. Lett.* **42**, 683 (2017).
 - [12] M. Schellhorn, G. Spindler, and M. Eichhorn, Improvement of the beam quality of a high-pulse-energy mid-infrared fractional-image-rotation-enhancement ZnGeP₂ optical parametric oscillator, *Opt. Lett.* **42**, 1185 (2017).
 - [13] A. A. Ionin, O. Kinyaevskiy, Y. M. Klimachev, V. A. Mozhaev, and Y. M. Andreev, Three-stage frequency conversion of sub-microsecond multiline CO laser pulse in a single ZnGeP₂ crystal, *Opt. Lett.* **43**, 3184 (2018).
 - [14] C.-P. Qian, B.-Q. Yao, B.-R. Zhao, G.-Y. Liu, X.-M. Duan, T.-Y. Dai, Y.-L. Ju, and Y.-Z. Wang, High repetition rate 102 W middle infrared ZnGeP₂ master oscillator power amplifier system with thermal lens compensation, *Opt. Lett.* **44**, 715 (2019).
 - [15] G.-Y. Liu, Y. Chen, B.-Q. Yao, R.-x. Wang, K. Yang, C. Yang, S.-y. Mi, T.-Y. Dai, and X.-M. Duan, 3.5 W long-wave infrared ZnGeP₂ optical parametric oscillator at 9.8 μm, *Opt. Lett.* **45**, 2347 (2020).
 - [16] S. Cheng, G. Chatterjee, F. Tellkamp, T. Lang, A. Ruehl, I. Hartl, and R. J. Dwayne Miller, Compact Ho:YLF-pumped ZnGeP₂-based optical parametric amplifiers tunable in the molecular fingerprint regime, *Opt. Lett.* **45**, 2255 (2020).
 - [17] S. D. Setzler, N. C. Giles, L. E. Halliburton, P. G. Schunemann, and T. M. Pollak, Electron paramagnetic resonance of a cation antisite defect in ZnGeP₂, *Appl. Phys. Lett.* **74**, 1218 (1999).
 - [18] S. D. Setzler, P. G. Schunemann, T. M. Pollak, M. C. Ohmer, J. T. Goldstein, F. K. Hopkins, K. T. Stevens, L. E. Halliburton, and N. C. Giles, Characterization of defect-related optical absorption in ZnGeP₂, *J. Appl. Phys.* **86**, 6677 (1999).
 - [19] N. Dietz, I. Tsveybak, W. Ruderman, G. Wood, and K. J. Bachmann, Native defect related optical properties of ZnGeP₂, *Appl. Phys. Lett.* **65**, 2759 (1994).
 - [20] L. Wang, L. Bai, K. T. Stevens, N. Y. Garces, N. C. Giles, S. D. Setzler, P. G. Schunemann, and T. M. Pollak, Luminescence associated with copper in ZnGeP₂, *J. Appl. Phys.* **92**, 77 (2002).
 - [21] N. C. Giles, L. Bai, M. M. Chirila, N. Y. Garces, K. T. Stevens, P. G. Schunemann, S. D. Setzler, and T. M. Pollak, Infrared absorption bands associated with native defects in ZnGeP₂, *J. Appl. Phys.* **93**, 8975 (2003).
 - [22] D. M. Hofmann, N. G. Romanov, W. Gehlhoff, D. Pfisterer, B. K. Meyer, D. Azamat, and A. Hoffmann, Optically detected magnetic resonance experiments on native defects in ZnGeP₂, *Physica B Condens. Matter* **340–342**, 978 (2003).
 - [23] M. Moldovan, K. T. Stevens, L. E. Halliburton, P. G. Schunemann, T. M. Pollak, S. D. Setzler, and N. C. Giles, Photoluminescence and EPR of phosphorus vacancies in ZnGeP₂, *MRS Proc.* **607**, 445 (2011).

- [24] Y. Yang, Y. Zhang, Q. Gu, H. Zhang, and X. Tao, Growth and annealing characterization of ZnGeP₂ crystal, *J. Cryst. Growth* **318**, 721 (2011).
- [25] G. Zhang, X. Tao, S. Wang, G. Liu, Q. Shi, and M. Jiang, Growth and thermal annealing effect on infrared transmittance of ZnGeP₂ single crystal, *J. Cryst. Growth* **318**, 717 (2011).
- [26] V. N. Brudnyi, D. L. Budnitskii, M. A. Krivov, R. V. Masagutova, V. D. Prochukhan, and Y. V. Rud, The electrical and optical properties of 2.0 MeV electron-irradiated ZnGeP₂, *Phys. Status Solidi A* **50**, 379 (1978).
- [27] G. Balčaitis, Z. Januškevičius, and A. Sodeika, On the nature of energy levels in ZnGeP₂, *Phys. Status Solidi A* **89**, K71 (1985).
- [28] X. Zhao, S. Zhu, B. Zhao, B. Chen, Z. He, R. Wang, H. Yang, Y. Sun, and J. Cheng, Growth and characterization of ZnGeP₂ single crystals by the modified Bridgman method, *J. Cryst. Growth* **311**, 190 (2008).
- [29] S. Xia, M. Wang, C. Yang, Z. Lei, G. Zhu, and B. Yao, Vertical bridgman growth and characterization of large ZnGeP₂ single crystals, *J. Cryst. Growth* **314**, 306 (2011).
- [30] G. C. Xing, K. J. Bachmann, and J. B. Posthill, High-pressure vapor transport of ZnGeP₂, *Appl. Phys. Lett.* **56**, 271 (1990).
- [31] G. K. Averkieva, V. S. Grigoreva, I. A. Maltseva, V. D. Prochukhan, and Y. V. Rud, Photoluminescence of p-type ZnGeP₂ crystals, *Phys. Status Solidi A* **39**, 453 (1977).
- [32] G. A. Verozubova, A. I. Gribenyukov, M. C. Ohmer, N. C. Fernelius, and J. T. Goldstein, Growth and characterization of epitaxial films of ZnGeP₂, *MRS Proceedings* **744**, M8.46 (2011).
- [33] Q. Fan, S. Zhu, B. Zhao, B. Chen, Z. He, J. Cheng, and T. Xu, Influence of annealing on optical and electrical properties of ZnGeP₂ single crystals, *J. Cryst. Growth* **318**, 725 (2011).
- [34] N. C. Giles, L. E. Halliburton, P. G. Schunemann, and T. M. Pollak, Photoinduced electron paramagnetic resonance of the phosphorus vacancy in ZnGeP₂, *Appl. Phys. Lett.* **66**, 1758 (1995).
- [35] M. H. Rakowsky, W. K. Kuhn, W. J. Lauderdale, L. E. Halliburton, G. J. Edwards, M. P. Scripsick, P. G. Schunemann, T. M. Pollak, M. C. Ohmer, and F. K. Hopkins, Electron paramagnetic resonance study of a native acceptor in as-grown ZnGeP₂, *Appl. Phys. Lett.* **64**, 1615 (1994).
- [36] W. Gehlhoff, R. N. Pereira, D. Azamat, A. Hoffmann, and N. Dietz, Energy levels of native defects in zinc germanium diphosphide, *Physica B Condens. Matter* **308–310**, 1015 (2001).
- [37] W. Gehlhoff, D. Azamat, and A. Hoffmann, EPR studies of native and impurity-related defects in II–IV–V₂ semiconductors, *Mater. Sci. Semicond. Process.* **6**, 379 (2003).
- [38] W. Gehlhoff, D. Azamat, A. Hoffmann, and N. Dietz, Structure and energy level of native defects in as-grown and electron-irradiated zinc germanium diphosphide studied by EPR and photo-EPR, *J. Phys. Chem. Solids* **64**, 1923 (2003).
- [39] W. Gehlhoff and A. Hoffmann, EPR identification of intrinsic and transition metal-related defects in ZnGeP₂ and other II–IV–V₂ compounds, *Physica B Condens. Matter* **404**, 4942 (2009).
- [40] A. Hoffmann, H. Born, A. Näser, W. Gehlhoff, J. Mafetone, D. Perlov, W. Ruderman, I. Zwieback, N. Dietz, and K. J. Bachmann, Native defect characterization in ZnGeP₂, *MRS Proc.* **607**, 373 (2000).
- [41] M. Moldovan and N. C. Giles, Broad-band photoluminescence from ZnGeP₂, *J. Appl. Phys.* **87**, 7310 (2000).
- [42] C. I. Rablau and N. C. Giles, Sharp-line luminescence and absorption in ZnGeP₂, *J. Appl. Phys.* **90**, 3314 (2001).
- [43] X. Jiang, M. S. Miao, and W. R. L. Lambrecht, Theoretical study of cation-related point defects in ZnGeP₂, *Phys. Rev. B* **71**, 205212 (2005).
- [44] X. Jiang, M. S. Miao, and W. R. L. Lambrecht, Theoretical study of the phosphorus vacancy in ZnGeP₂, *Phys. Rev. B* **73**, 193203 (2006).
- [45] X. Jiang and W. R. L. Lambrecht, Jahn–teller distortion of the zinc vacancy in ZnGeP₂, *Chinese Phys. Lett.* **25**, 1075 (2008).
- [46] X. Jiang and W. R. L. Lambrecht, The importance of the self-interaction correction for jahn–teller distortion of the zinc vacancy in ZnGeP₂, *Solid State Commun.* **149**, 685 (2009).
- [47] N. Dietz, W. Busse, H. E. Gumlich, W. Ruderman, I. Tsveybak, G. Wood, and K. J. Bachmann, Defect characterization in ZnGeP₂ by time-resolved photoluminescence, *MRS Proc.* **450**, 333 (2011).
- [48] U. Kaufmann, J. Schneider, and A. Räuber, ESR detection of antisite lattice defects in GaP, CdSiP₂, and ZnGeP₂, *Appl. Phys. Lett.* **29**, 312 (1976).
- [49] P. Zapol, R. Pandey, M. Ohmer, and J. Gale, Atomistic calculations of defects in ZnGeP₂, *J. Appl. Phys.* **79**, 671 (1996).
- [50] V. N. Brudnyi, V. G. Voevodin, and S. N. Grinyaev, Deep levels of intrinsic point defects and the nature of “anomalous” optical absorption in ZnGeP₂, *Phys. Solid State* **48**, 2069 (2006).
- [51] S. Chen, P. Narang, H. A. Atwater, and L.-W. Wang, Phase stability and defect physics of a ternary ZnSnN₂ semiconductor: First principles insights, *Adv. Mater.* **26**, 311 (2014).
- [52] N. Tsunoda, Y. Kumagai, A. Takahashi, and F. Oba, Electrically Benign Defect Behavior in Zinc Tin Nitride Revealed From First Principles, *Phys. Rev. Appl.* **10**, 011001 (2018).
- [53] D. Skachkov, A. Punya Jaroenjittichai, L.-y. Huang, and W. R. L. Lambrecht, Native point defects and doping in ZnGeN₂, *Phys. Rev. B* **93**, 155202 (2016).
- [54] N. L. Adamski, Z. Zhu, D. Wickramaratne, and C. G. Van de Walle, Hybrid functional study of native point defects and impurities in ZnGeN₂, *J. Appl. Phys.* **122**, 195701 (2017).
- [55] Y. Kumagai, M. Choi, Y. Nose, and F. Oba, First-principles study of point defects in chalcopyrite ZnSnP₂, *Phys. Rev. B* **90**, 125202 (2014).
- [56] X. Wu, F. Meng, D. Chu, M. Yao, K. Guan, D. Zhang, and J. Meng, Carrier tuning in ZnSnN₂ by forming amorphous and microcrystalline phases, *Inorg. Chem.* **58**, 8480 (2019).

- [57] S. Nakatsuka, N. Yuzawa, J. Chantana, T. Minemoto, and Y. Nose, Solar cells using bulk crystals of rare metal-free compound semiconductor ZnSnP₂, *Phys. Status Solidi A* **214**, 1600650 (2017).
- [58] M. A. Ryan, M. W. Peterson, D. L. Williamson, J. S. Frey, G. E. Maciel, and B. A. Parkinson, Metal site disorder in zinc tin phosphide, *J. Mater. Res.* **2**, 528 (2011).
- [59] G. Kresse and J. Hafner, Ab initio molecular dynamics for liquid metals, *Phys. Rev. B* **47**, 558 (1993).
- [60] J. Heyd and G. E. Scuseria, Efficient hybrid density functional calculations in solids: Assessment of the Heyd–Scuseria–Ernzerhof screened Coulomb hybrid functional, *J. Chem. Phys.* **121**, 1187 (2004).
- [61] J. Heyd, J. E. Peralta, G. E. Scuseria, and R. L. Martin, Energy band gaps and lattice parameters evaluated with the Heyd–Scuseria–Ernzerhof screened hybrid functional, *J. Chem. Phys.* **123**, 174101 (2005).
- [62] G. Kresse and D. Joubert, From ultrasoft pseudopotentials to the projector augmented-wave method, *Phys. Rev. B* **59**, 1758 (1999).
- [63] P. E. Blöchl, Projector augmented-wave method, *Phys. Rev. B* **50**, 17953 (1994).
- [64] H. J. Monkhorst and J. D. Pack, Special points for Brillouin-zone integrations, *Phys. Rev. B* **13**, 5188 (1976).
- [65] C. G. Van de Walle and J. Neugebauer, First-principles calculations for defects and impurities: Applications to III-nitrides, *J. Appl. Phys.* **95**, 3851 (2004).
- [66] C. Freysoldt, B. Grabowski, T. Hickel, J. Neugebauer, G. Kresse, A. Janotti, and C. G. Van de Walle, First-principles calculations for point defects in solids, *Rev. Mod. Phys.* **86**, 253 (2014).
- [67] G. Makov and M. C. Payne, Periodic boundary conditions in ab initio calculations, *Phys. Rev. B* **51**, 4014 (1995).
- [68] S. Lany and A. Zunger, Assessment of correction methods for the band-gap problem and for finite-size effects in supercell defect calculations: Case studies for ZnO and GaAs, *Phys. Rev. B* **78**, 235104 (2008).
- [69] C. Freysoldt, J. Neugebauer, and C. G. Van de Walle, Fully Ab Initio Finite-Size Corrections for Charged-Defect Supercell Calculations, *Phys. Rev. Lett.* **102**, 016402 (2009).
- [70] See the Supplemental Material at <http://link.aps.org/supplemental/10.1103/PhysRevApplied.15.024035> for the chemical-potential region calculated by different functionals, the atomic configuration of interstitial defects, a configuration coordinate diagram, and a comparison of correction schemes for charged defects.
- [71] J. Ma, S.-H. Wei, T. A. Gessert, and K. K. Chin, Carrier density and compensation in semiconductors with multiple dopants and multiple transition energy levels: Case of Cu impurities in CdTe, *Phys. Rev. B* **83**, 245207 (2011).
- [72] J.-H. Yang, J.-S. Park, J. Kang, W. Metzger, T. Barnes, and S.-H. Wei, Tuning the Fermi level beyond the equilibrium doping limit through quenching: The case of CdTe, *Phys. Rev. B* **90**, 245202 (2014).
- [73] X. Yan, P. Li, L. Kang, S.-H. Wei, and B. Huang, First-principles study of electronic and diffusion properties of intrinsic defects in 4H-SiC, *J. Appl. Phys.* **127**, 085702 (2020).
- [74] S. Chen, A. Walsh, X.-G. Gong, and S.-H. Wei, Classification of lattice defects in the kesterite Cu₂ZnSnS₄ and Cu₂ZnSnSe₄ earth-abundant solar cell absorbers, *Adv. Mater.* **25**, 1522 (2013).
- [75] A. M. Stoneham, *Theory of Defects in Solids: Electronic Structure of Defects in Insulators and Semiconductors* (Oxford University Press, Oxford, 2001).
- [76] A. Alkauskas, B. B. Buckley, D. D. Awschalom, and C. G. Van de Walle, First-principles theory of the luminescence lineshape for the triplet transition in diamond NV centres, *New J. Phys.* **16**, 073026 (2014).
- [77] F. Schanovsky, W. Göts, and T. Grasser, Multiphonon hole trapping from first principles, *J. Vac. Sci. Technol. B* **29**, 01A201 (2011).
- [78] A. Alkauskas, J. L. Lyons, D. Steiauf, and C. G. Van de Walle, First-Principles Calculations of Luminescence Spectrum Line Shapes for Defects in Semiconductors: The Example of GaN and ZnO, *Phys. Rev. Lett.* **109**, 267401 (2012).
- [79] K. Huang, Lattice relaxation and multiphonon transitions, *Contemp. Phys.* **22**, 599 (1981).
- [80] B. R. Pamplin, T. Kiyosawa, and K. Masumoto, Ternary chalcopyrite compounds, *Prog. Cryst. Growth Charact. Mater.* **1**, 331 (1979).
- [81] K. V. Shportko, Optical phonon behaviors in ZnGeP₂ single crystals from temperature dependent far-infrared reflectance spectra, *Vib. Spectrosc.* **80**, 1 (2015).
- [82] A. V. Krivosheeva, V. L. Shaposhnikov, V. V. Lyskouski, V. E. Borisenko, F. A. d'Avitaya, and J. L. Lazari, Prospects on Mn-doped ZnGeP₂ for spintronics, *Microelectron. Reliab.* **46**, 1747 (2006).
- [83] S. Limpijumnong, W. R. L. Lambrecht, and B. Segall, Electronic structure of ZnGeP₂: A detailed study of the band structure near the fundamental gap and its associated parameters, *Phys. Rev. B* **60**, 8087 (1999).
- [84] R. Cao, H.-X. Deng, J.-W. Luo, and S.-H. Wei, Origin of the anomalous trends in band alignment of GaX/ZnGeX₂ (X = N, P, As, Sb) heterojunctions, *J. Semicond.* **40**, 042102 (2019).
- [85] J. P. Perdew, K. Burke, and M. Ernzerhof, Generalized Gradient Approximation Made Simple, *Phys. Rev. Lett.* **77**, 3865 (1996).
- [86] D. M. Ceperley and B. J. Alder, Ground State of the Electron Gas by a Stochastic Method, *Phys. Rev. Lett.* **45**, 566 (1980).
- [87] R. Bendorius, V. D. Prochukhan, and A. Šileika, The lowest conduction band minima of A₂B₄C-type semiconductors, *Phys. Status Solidi B* **53**, 745 (1972).
- [88] M. C. Petcu, N. C. Giles, P. G. Schunemann, and T. M. Pollak, Band-Edge photoluminescence at room temperature from ZnGeP₂ and AgGaSe₂, *Phys. Status Solidi B* **198**, 881 (1996).
- [89] B. Zhang, X. Zhang, J. Yu, Y. Wang, K. Wu, and M.-H. Lee, First-Principles high-throughput screening pipeline for nonlinear optical materials: Application to borates, *Chem. Mater.* **32**, 6772 (2020).
- [90] S.-R. Zhang, S.-F. Zhu, L.-H. Xie, X.-W. Chen, and K.-H. Song, Theoretical study of the structural, elastic and thermodynamic properties of chalcopyrite ZnGeP₂, *Mater. Sci. Semicond. Process.* **38**, 41 (2015).

- [91] J. Dutkiewicz, The P-Zn (Phosphorus-Zinc) system, *J. Phase Equilibria* **12**, 435 (1991).
- [92] V. Stevanović, S. Lany, X. Zhang, and A. Zunger, Correcting density functional theory for accurate predictions of compound enthalpies of formation: Fitted elemental-phase reference energies, *Phys. Rev. B* **85**, 115104 (2012).
- [93] M. R. Ranade, F. Tessier, A. Navrotsky, V. J. Leppert, S. H. Risbud, F. J. DiSalvo, and C. M. Balkas, Enthalpy of formation of gallium nitride, *J. Phys. Chem. B* **104**, 4060 (2000).
- [94] Q. Yan, A. Janotti, M. Scheffler, and C. G. Van de Walle, Role of nitrogen vacancies in the luminescence of Mg-doped GaN, *Appl. Phys. Lett.* **100**, 142110 (2012).
- [95] N. L. Adamski, Z. Zhu, D. Wickramaratne, and C. G. Van de Walle, Optimizing n-type doping of ZnGeN₂ and ZnSiN₂, *Phys. Rev. B* **100**, 155206 (2019).
- [96] D. Yang, B. Zhao, B. Chen, S. Zhu, Z. He, W. Huang, Z. Zhao, and M. Liu, Impurity phases analysis of ZnGeP₂ single crystal grown by Bridgman method, *J. Alloys Compd.* **709**, 125 (2017).
- [97] S. B. Zhang and J. E. Northrup, Chemical Potential Dependence of Defect Formation Energies in GaAs: Application to Ga Self-Diffusion, *Phys. Rev. Lett.* **67**, 2339 (1991).
- [98] J. L. Lyons and C. G. Van de Walle, Computationally predicted energies and properties of defects in GaN, *npj Comput. Mater.* **3**, 12 (2017).
- [99] A. P. Seitsonen, R. Virkkunen, M. J. Puska, and R. M. Nieminen, Indium and phosphorus vacancies and antisites in InP, *Phys. Rev. B* **49**, 5253 (1994).
- [100] A. Janotti and C. G. Van de Walle, Native point defects in ZnO, *Phys. Rev. B* **76**, 165202 (2007).